RSC Advances

PAPER

View Article Online
View Journal | View Issue

Cite this: *RSC Adv.*, 2023, **13**, 13930

Novel Mn_4-Co_2 nanocluster@photosensitizers/SalenCo(III) catalyze the copolymerization of carbon dioxide and propylene oxide†

ZhiWei Yang and LongChao Du *

Received 16th March 2023
Accepted 24th April 2023

DOI: 10.1039/d3ra01742g

rsc.li/rsc-advances

In general, transition metals (TMs) often facilitate highly efficient catalysis. Herein, we synthesized a series of nanocluster composite catalysts by combining with photosensitizers and SalenCo(III) for the first time and studied the catalytic copolymerization of CO_2 and propylene oxide (PO). Systematic experiments have shown that the selectivity of copolymerization products can be improved by the nanocluster composite catalysts, and their synergistic effects significantly improved the photocatalytic performance of carbon dioxide copolymerization. At specific wavelengths, **I@S1** can achieve a TON of 536.4, which is 2.26 times that of **I@S2**. Interestingly, in the photocatalytic products of **I@R2**, CPC reached 37.1%. These findings provide a new idea for the study of TM nanocluster@photosensitizers for carbon dioxide photocatalysis, and may provide guidance for exploring low cost and highly efficient carbon dioxide emission reduction photocatalysts.

1. Introduction

Being one of the major component of greenhouse gases, CO_2 has damaged the ecological balance of nature and threatened the survival of a wide range of organisms.[1] However, the cheap, rich nature of CO_2 has made it an important research direction in society. The process of converting CO_2 into polycarbonate has been widely studied and has entered industrial systems.[2–5] Polycarbonate is a biodegradable material with many environmental, biomedical and medical applications.[6] They are synthesized by means of the alternating copolymerization of CO_2 and epoxy compounds, such as cyclohexene oxide (CHO) and PO.[7–10] A number of catalyst systems based on different metals is used to synthesize polycarbonate and five-headed cyclic carbonate (Scheme 1). However, due to the thermodynamic stability of CO_2, highly active catalysts are required for CO_2 conversion.[11–15]

Schiff base was first developed in 1864, and Hugo Schiff synthesized it using salicylaldehyde, aniline, and copper ions. Compounds with an imine group were referred to as Schiff bases. Schiff base itself can be used as a catalyst for the cycloaddition response of carbon dioxide and epoxy compounds.[16] Some binding complexes with transition metals can significantly enhance their catalytic activity, which are mainly composed of metal elements, such as Mn and Co.[17–19] Therefore, the improvement of Salen-type complexes with Schiff base as ligands has attracted significant research interest. Vagin Sergei I. and his colleagues discovered a series of Salen-Cr(III) bifunctional catalysts.[20] These catalysts have high activity and good high-temperature resistance in the copolymerization of carbon dioxide and epoxide, and enabled the production of the polymer polycarbonate and polyether.[21] Charlotte K. Williams *et al.* synthesized a magnesium-based catalyst with good performance in 2012. The produced cyclohexene carbonate has >99% selectivity and a carbonate bond. In addition, they can be used with water to effectively produce polycarbonate polyols.[22–25] Charlotte K. Williams and others designed bimetallic heteronuclear catalysts in 2018. Compared with related mononuclear analogues, the Zn/Co catalyst has excessive catalytic stability, effort and selectivity in heteronuclear complexes.[26]

Metal nanoclusters (size < 2 nm) have attracted considerable attention owing to their special small size properties. In this ultra-small dimensional variant, the nanoclusters lose their plasma characteristics and display molecular shells.[27] In the past few years, metal nanoclusters have been extensively studied owing to their various packaging forms, including catalysis, doping, sensing, biomedicine, and photovoltaic panels. In many cases, the atomic structure of nanoclusters has been studied as the key to understanding their special physical and chemical properties.[28] However, the lack of reliable characterization ability is one of the reasons hindering us from understanding the arrangement of atomic clusters, especially on the surface of metal ligands. Therefore, in cluster chemistry, how to determine the basic structure of nanoclusters is still a very good challenge.[29] At the same time, adjusting the surface ligands of metal nanoclusters plays an important role in

School of Chemistry and Chemical Engineering & the Key Laboratory of Environment-friendly Polymer Materials of Anhui Province, Key Laboratory of Structure and Functional Regulation of Hybrid Materials, Anhui University, Ministry of Education, Hefei 230601, PR China. E-mail: dulongchao@sina.com

† Electronic supplementary information (ESI) available. CCDC 2224970. For ESI and crystallographic data in CIF or other electronic format see DOI: https://doi.org/10.1039/d3ra01742g

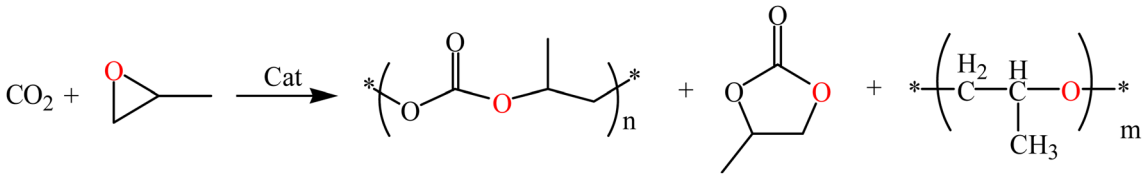

Scheme 1 Copolymerization route: CO_2 and PO copolymerization catalyzed by a catalyst.

adjusting their size, structure and properties at the atomic level. It is well known that due to the difference between clusters and blocks, clusters have a larger surface-to-volume ratio and often have more unique properties in geometric and electronic structures.[30–32]

Metal cluster catalysts exhibit incredible overall performance in heterogeneous catalysis. Theoretical research and experimental evidence have shown that the use of some transition metallic dimer sites can enhance the catalytic performance. For example, Kun Huang *et al.*[33] synthesized the copper cluster complexes $\{2Cu(L)(A)\cdot 3H_2O\}_n$ (L = bis(4-(4*H*-1,2,4-triazol-4-yl) phenyl)methane, A = deprotonation 1,4-naphthalene dicarboxylic acid), as a heterogeneous catalyst for the chemical fixation of CO_2 because their high internal surface area and open metal sites can easily improve the catalytic activity. This study shows that the complex can be used as an efficient heterogeneous catalyst to convert CO_2 into cyclic carbonate under the conditions of 1 atm CO_2 and solvent-free conditions, with the yield of 81.0–99.0%. In addition, it still maintains good catalytic efficiency (83.0% conversion) after 10 cycles. The natural Mn_4Ca clusters in photosystem II can serve as a blueprint for the improvement of synthetic water-splitting catalysts for producing photovoltaic fuels in photosynthesis.[34] Although considerable progress has been made, it is still a difficult challenge to cultivate synthetic clusters that can accurately simulate the shape and characteristics of biocatalysts.[35,36] Here, a new Mn_4-Co_2 nanocluster and two SalenCo(III) catalysts were synthesized for the first time. The effect of photocatalysis on the copolymerization of carbon dioxide and PO was discussed together with two dyes, and the synergistic catalytic effect of these composite catalysts was also discussed.

2. Experimental section

2.1 Chemicals

All synthesis manipulations were carried out under aerobic condition. All organic solvents were dried by using a 4A molecular sieve. Acetonitrile and PO were further purified by distillation over CaH_2. All other chemicals were used as received without further purification. $Bu^n_4NMnO_4$ was prepared according to the procedure reported previously.[37] Caution! $Bu^n_4NMnO_4$ is potentially explosive and should be used only in small quantities.

2.2 Synthesis and characterization

2.2.1 Synthesis of compound 1. 1,2-Cyclohexanediamine (1.44 g, 12.6 mmol), potassium carbonate (3.5 g, 25.3 mmol) and 15 mL distilled water were added successively into a 250 mL three-necked flask equipped with a stirrer, a reflux condenser tube and a constant pressure drip funnel, and stirred to dissolve them completely. Then, 60 mL ethanol was added, the reaction solution became white with turbidity, and it was then heated to reflux. 5-*tert*-Butylsalicylaldehyde ethanol solution (6.04 g, 25.3 mmol, 25 mL ethanol) was then added evenly within 30 minutes, and then the inner wall of the drip funnel was rinsed with 25 mL ethanol after dripping. The mixture was refluxed for 2 hours under vigorous stirring, and then the heating was stopped. A total volume of 70 mL of distilled water was then added, and the mixture was further mixed continuously for 2 hours. The mixture was cooled to below 5 °C and held for 1 hour, then filtered by suction. The filter cake was dissolved in 250 mL dichloromethane, and then saturated brine (50 mL) and distilled water (2 × 150 mL) were used. The mixture was dried with anhydrous sodium sulfate, the solvent was removed in vacuum, and the product was recrystallized with ethanol to obtain 5.81 g yellow powder in 95% yield.

^{1}H-NMR (400 MHz, DMSO-d_6) δ = 13.03 (s, 2H), 8.44 (s, 2H), 7.28 (s, 2H), 7.26 (d, J = 2.2 Hz, 2H), 7.25 (d, J = 2.4 Hz, 2H), 6.71–6.67 (d, 2H), 1.80 (dd, J = 26.4, 10.8 Hz, 4H), 1.58–1.42 (t, J = 10.2 Hz, 4H), 1.16 (s, 18H). ^{13}C-NMR (400 MHz, DMSO-d_6) δ 165.96 (C–CH), 158.57 (aryl C), 141.29 (aryl C), 129.93 (aryl C), 128.35 (aryl C), 118.34 (aryl C), 116.39 (aryl C), 72.05 (C–CH), 40.69, 40.48, 40.27, 40.07, 39.86, 39.65, 39.44, 34.19, 33.18 (C–CH_{2-}), 31.69 (C–3CH_3), 24.29 (C–CH_{2-}) MS: m/z 435.30 for $C_{28}H_{38}N_2O_2$, found 435.3046 (Fig. S1†).

2.2.2 Synthesis of compound 2. *o*-Phenylenediamine (0.9702 g, 8.987 mmol) was added to a three-necked flask, then 35 mL absolute ethanol was added. Finally, 5-(*tert*-butyl)-2-hydroxybenzaldehyde (3.2032 g, 19.14 mmol) was added. Nitrogen was introduced for protection, and the reaction proceeded for 36 hours. After the reaction, compound 2 was filtered to obtain an orange solid in yield (7 g, 65.6%).

^{1}H-NMR (400 MHz, Chloroform-d_6) δ = 13.70, (s, 2H), 8.65 (s, 2H), 7.37–7.32 (dd, J = 5.9, 3.4 Hz, 2H), δ = 7.22, (s, 2H), 7.24–7.20 (m, 2H), 7.12–6.97 (m, 2H), 6.92–6.76 (m, 2H), 1.42 (d, J = 3.4 Hz, 18H); ^{13}C-NMR (400 MHz, DMSO-d_6) δ 162.05 (C–CH), 158.23 (aryl C), 143.06 (aryl C), 128.99 (aryl C), 128.19 (aryl C), 119.70 (aryl C), 118.86 (aryl C), 117.28 (aryl C), 116.56 (aryl C), 115.81 (aryl C), 40.70, 40.49, 40.07, 39.86, 39.65, 39.44, 34.33, 31.76 (C–3CH_3). MS: m/z 429.25 for $C_{28}H_{32}N_2O_2$, found 429.2530 (Fig. S2†).

2.2.3 Synthesis of S1. Compound **1** (2.0 mmol, 0.8686 g) was dissolved in 25 mL of dichloromethane, and added into a three-necked flask. Meanwhile, anhydrous cobalt acetate (2.1 mmol, 0.3718 g) was added to a beaker and dissolved in 20 mL ethanol. The cobalt acetate ethanol solution was slowly

added into the three-necked flask through a constant pressure funnel. Then, 4-(imidazol-1-yl) phenol (2.0 mmol, 0.320 g) was added and dissolved in 25 mL dichloromethane, and dropped into the above cobalt solution with stirring and continuous oxygen supply at room temperature. After the reaction, the solution was filtered and spun dry to obtain the product (0.74 g; 48.7%).

^{1}H-NMR (400 MHz, DMSO-d_6) δ = 8.72 (d, J = 6.5 Hz, 2H), 8.24 (s, 2H), 8.06 (d, J = 1.9 Hz, 2H), 7.72 (d, J = 8.1 Hz, 2H), 7.43 (m, 2H), 7.34 (d, J = 7.5, 1.7 Hz, 1H), 6.92 (t, J = 7.2 Hz, 2H), 6.77 (d, J = 6.7 Hz, 1H), 6.60 (dt, J = 7.6 Hz, 1H), 2.79 (d, J = 11.1 Hz, 2H), 2.24 (d, J = 7.5 Hz, 2H), 1.87 (dt, J = 11.1 Hz, 2H), 1.79 (d, J = 7.6 Hz, 2H), 1.73–1.55 (m, 4H), 1.55 (s, 9H), 1.40 (s, 9H), 0.89 (t, J = 7.3 Hz, 2H), 0.80 (t, 3H). MS: m/z calcd for $C_{37}H_{40}N_4O_3Co_1$: 650.27, found 651.08 (Fig. S3†).

2.2.4 Synthesis of S2. Using the same method as above, **S2** was synthesized and the product is 0.81 g; 53.3%.

^{1}H-NMR (400 MHz, DMSO-d_6) δ 8.40 (s, 2H), 7.51 (d, 2H), 7.45 (d, J = 14.2, 1.7 Hz, 2H), 7.39 (d, 1H), 7.31 (d, 2H), 7.25–7.10 (m, 2H), 6.93 (t, 2H), 6.73 (d, 2H), 6.53–6.37 (m, 2H), 1.47 (s, 18H). MS: m/z calcd for $C_{37}H_{34}N_4O_3Co_1$: 645.22, found 645.93 (Fig. S4†).

2.2.5 Synthesis of cluster $[Mn_4Co_2O_2(Bu^tCO_2)_{10}(C_5H_5N)_4]$ (I). Cluster **I** was synthesized by mixing $(MnCH_3CO_2)_2\cdot 4(H_2O)$ (0.1225 g, 0.5 mmol), $Co(NO_3)_2\cdot 6(H_2O)$ (0.145 g, 0.5 mmol), $Bu^n{}_4NMnO_4$ (0.723 g, 2 mmol) and pivalic acid (2.04 g, 20.0 mmol) in boiling acetonitrile (100 mL) that was stirred at high speed to obtain a dark brown solution, which was then filtered to remove the precipitate. Reddish-brown crystals (0.92 g, precursor of cluster **I**) were formed within four days at room temperature. In the presence of 2% pyridine (v/v), 0.588 g of the precursor of cluster **I** was dissolved in 9 mL of ethyl acetate.[38] The black red crystal (0.184 g) of clusters **I** was formed after several days at −10 °C, with a yield of 22% (on Co basis). Crystal and refinement data for clusters **I**: $C_{70}H_{110}Co_2Mn_4N_4O_{22}$, 1697.23 (Table S1†). MS: m/z found 1698.77 (Fig. S5†). iCP MS: Mn, 1022.96 μg L^{-1}; Co, 602.78 μg L^{-1} iCP AES: Mn, 0.85 μg mL^{-1}; Co, 0.43.78 μg mL^{-1}.

2.3 Copolymerization

In an external illumination-type autoclave, the photocatalysis of the carbon dioxide copolymerization was carried out by stable stirring at a specific temperature. In a typical experiment, a 100 mL autoclave was used to heat to 60 °C under vacuum for reaction for 12 hours, and then cooled to room temperature under vacuum. The combination of cluster **I** and photosensitizer was dissolved in PO. The mixture solution was injected into an autoclave equipped with a magnetic stirrer under CO_2 atmosphere, which operates under CO_2 atmosphere. The autoclave is usually heated to 60 °C and the CO_2 pressure is 2 MPa. The mixture is stirred at 60 °C for the specified reaction time, then cooled to room temperature and ventilated in a fume hood. The reaction group mixture is filtered by silica gel pad to eliminate the catalyst residue. The copolymer is dried to a stable weight in a vacuum oven. A small aliquot of the resultant copolymerization mixture was removed from the reactor for ^{1}H-NMR analysis. For the photo-blocking polymerization experiment, an opaque black cloth was used to cover the quartz glass. In the experiment of photopolymerization, an external light source was introduced and a 100 W incandescent lamp was used for illumination. The distance between the light source and the reactor quartz glass is 20 cm. Light of other wavelengths is filtered by the filter to obtain the required wavelength (±18 nm; transmissivity> 90%).

3. Results and discussion

3.1 Synthesis and characterization

Based on the previous research results, we know that the Salen metal catalyst system shows good activity and efficiency for the copolymerization of CO_2 and epoxy compounds. Therefore, our main goal is to synthesize new ligands and explore the electronic effects of different diamines and introduced metal nanoclusters on the copolymerization of carbon dioxide and PO.

The first step is the preparation of Schiff base ligands. Schiff bases were synthesized from 5-*tert*-butyl-2-

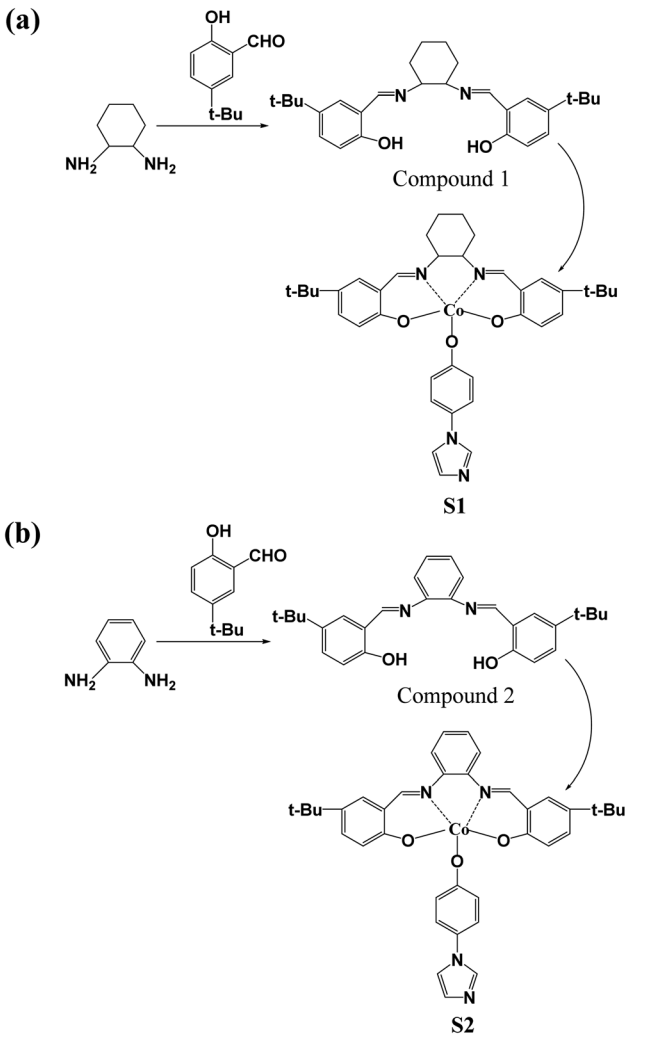

Scheme 2 (a) Synthesis route of compound **1** and **S1**. (b) Synthesis route of compound **2** and **S2**.

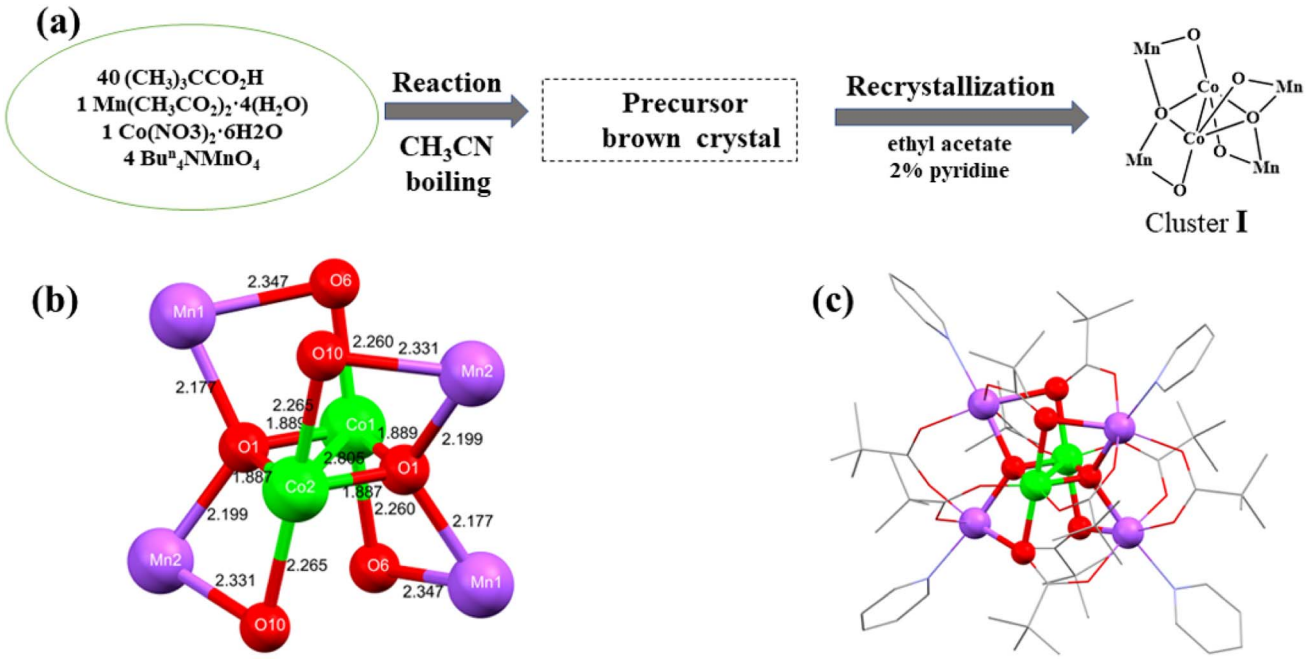

Fig. 1 Crystal structures of the Mn_4Co_2 clusters **I** and the synthetic route. (a) The synthetic route. Mn, Co, O, N, and C are shown in purple, green, red, lavender, and black, respectively. For clarity, all H atoms are omitted. (b) The $Mn_4Co_2O_6$ core of clusters I. (c) Structure of clusters I, including all ligand groups.

hydroxybenzaldehyde with 1,2-cyclohexanediamine and *o*-phenylenediamine at room temperature in ethanol, respectively. The condensation reaction between the aldehyde groups and amines is a key step in the synthesis of the required Salen ligands (compounds **1** and **2**). At this point, we have synthesized two Schiff bases with different functional groups. The ligand reacts with cobalt acetate to form a Salen metal complex, which is then oxidized to Co^{3+} by introducing O_2 into the solution. The condition can support the oxidation of Co(II) to Co(III) during the reaction process. Subsequently, the O–H bond was destroyed and catalysts **S1** and **S2** were formed, respectively (Scheme 2). The ^{1}H-NMR, ^{13}C-NMR spectra and mass spectra of compounds **1** and **2** are shown in Fig. S1 and S2.† The ^{1}H-NMR spectra and mass spectra of catalysts **S1** and **S2** are shown in Fig. S3 and S4.†

Here, we have synthesized a new Mn–Co nanocluster **I** containing a $Mn_4Co_2O_4$ hexametallic skeleton and all types of μ-oxido fractions observed at OEC.[39] The cluster was synthesized in the presence of excess neopentanoic acid in boiling acetonitrile in a 4 : 1 : 1 molar ratio from the reaction of $Bu^n_4NMnO_4$, $Mn(CH_3CO_2)_2\cdot4(H_2O)$ and $Co(NO_3)_2\cdot6(H_2O)$. On cooling, reddish brown crystals were formed and further recrystallized

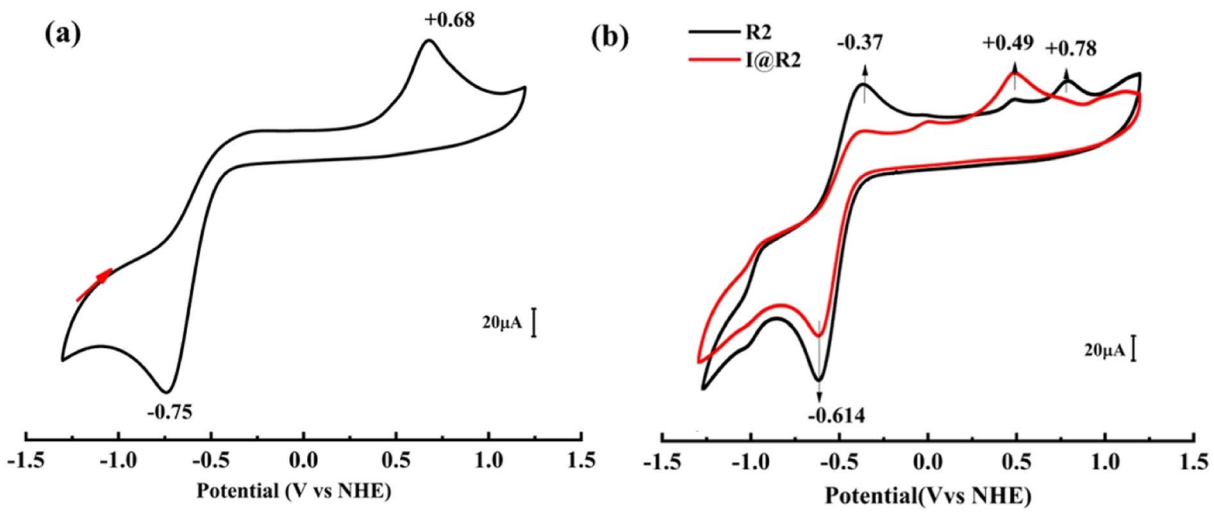

Fig. 2 (a) CV measurements of clusters I; the arrows indicate the scan direction. (b) CV measurements of R2 and I@R2.

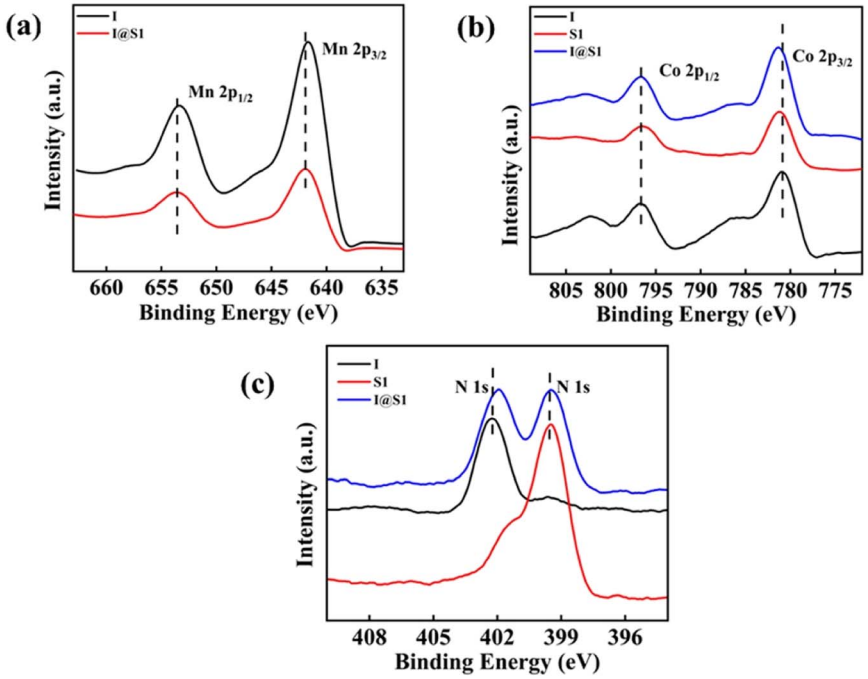

Fig. 3 (a) Mn 2p, (b) Co 2p, (c) N 1s.

in the presence of 2% pyridine in ethyl acetate solution. The final product of cluster **I** $[Mn_4Co_2O_2(Bu^tCO_2)_{10}(C_5H_5N)_4]$ was obtained.

The crystal structure and metal core of cluster **I** is shown in Fig. 1, and consists of a six-metal core and four protected pyridines, ten carboxylates, two cobalt atoms and two oxygen atoms forming a plane. The equatorial plane angles $O1^1$–Co1–Co2, O1–Co1–Co2, $O1^1$–Co1–O1 and $O1^1$–Co2–Co1, O1–Co2–Co1, $O1^1$–Co2–O1 bond angles are 41.97(7)°, 41.98(7)°, 83.95(15)° and 42.05(7)°, 42.05(7)°, 84.11(15)° respectively. The central cobalt atom Co1 has bond lengths of 2.8053(11) Å, 1.889(2) Å, 1.889(2) Å, 2.260(3) Å, 2.260(3) Å to Co2, O1, $O1^1$, O6, $O6^1$, respectively. There are four centrosymmetric Mn atoms in the periphery, $O1^1$–Mn1–$O6^1$, Co1–O1–$Mn1^1$, Co1–O1– $Mn2^1$, and $Mn1^1$–O1–$Mn2^1$ with bond angles of 77.16(9)°, 102.81(11)°, 118.62(12)°, and 117.51(14)°, respectively. The bond lengths of the outer Mn1 atom to $O1^1$, $O6^1$ are 2.177(3) Å, 2.346(3) Å, respectively. In addition, the cluster exhibits a redox potential at +0.68 V *vs.* NHE (Fig. 2) and as can be seen in Fig. 3, the maximum absorption peak in the visible range of cluster **I** is at 493 nm, indicating its potential as a good synthetic model for OEC (Table 1).

3.2 Cyclic voltammetry experiments and X-ray photoelectron spectra

In order to further understand the synergistic effect of cluster **I** and different photosensitizers (**R1** and **R2**), the electrochemical study using cyclic voltammetry (CV) was conducted. Firstly, the electrochemical behaviors of **I**, **R2** and **I@R2** were studied, the

Table 1 Synthesis and naming of composite catalysts

	Type (catalyst)	Synthetic route	Name
Pho 1	4-(4-Diethylaminophenylazo)pyridine	—	**R1**
Pho 2	4-Styrylpyridine	—	**R2**
Cat 1	Mn_4-Co_2 nanocluster	Fig. 1a	**I**
Cat 2	Pho 1 + Mn_4-Co_2 nanocluster	**R1** : **I** = 1 : 1[a]	**I@R1**
Cat 3	Pho 2 + Mn_4-Co_2 nanocluster	**R2** : **I** = 1 : 1	**I@R2**
Cat 4	SalenCo(III)	Scheme 2a	**S1**
Cat 5	SalenCo(III)	Scheme 2b	**S2**
Cat 6	Cat 4 + Mn_4-Co_2 nanocluster	**S1** : **I** = 1 : 1	**I@S1**
Cat 7	Cat 5 + Mn_4-Co_2 nanocluster	**S2** : **I** = 1 : 1	**I@S2**
Cat 8	**I@S1** post-catalytic recovery	—	**I@S1(1)**
Cat 9	**I@S1** recycle after 3 cycles	—	**I@S1(3)**
Cat 10	**I@S1** recycle after 5 cycles	—	**I@S1(5)**

[a] Catalyst: Mn_4-Co_2 nanocluster + SalenCo(III)/Pho = 1 : 1 (molar ratio); Pho = Photosensitizer.

electrolyte solution was 0.1 M $Bu^n{}_4NPF_6$ in a 3 : 2 ratio of 1,2-dichloroethane/ethyl acetate. As shown in Fig. 2a, it is seen that **I** has an oxidation peak (E_{pa} = +0.68 V) and a reduction peak (E_{pc} = −0.75 V). From Fig. 2b, it can be seen that the **R2** has two oxidation peaks (E_{pa1} = −0.37 V, E_{pa2} = +0.78 V) and only one reduction peak (E_{pc} = −0.614 V). Compared with **I** and **R2**, the reduction peak (E_{pc} = −0.614 V) of **I@R2** is consistent with **R2**, and the oxidation peak of **I@R2** (E_{pa} = +0.49 V) is lower than that of **I**. A significant reduction in the potential difference between redox peaks improves the kinetic and thermodynamic properties of electrochemical reactions, thus increasing the efficiency and controllability of the photoelectrochemical reactions. To further understand the synergistic effect of cluster **I** and Schiff base complex **S1**, the chemical state and binding energy of the single-component catalyst cluster **I**, **S1** and the composite catalyst **I@S1** were determined by X-ray photoelectron spectroscopy (XPS) after the photocatalytic copolymerization reaction. The XPS spectrum of Mn 2p is shown in Fig. 3a. Compared with the metal Mn $2p_{1/2}$ (653.3 eV) and Mn $2p_{3/2}$ (641.7 eV) in cluster I, the peaks of Mn $2p_{1/2}$ and Mn $2p_{3/2}$ in the composite catalyst shifted forward by about 0.3 eV. Similarly, as shown in Fig. 3b, the peak of Co $2p_{1/2}$ and Co $2p_{3/2}$ of the composite catalyst shifted forward by about 0.2 eV, which is attributed to the strong electronic effect caused by the action of cluster **I** on the Schiff base complex. As shown in Fig. 3c, compared with N 1s (402.25 eV) in cluster **I**, the N 1s (401.95 eV) corresponding to the composite catalyst shifted negatively by about 0.3 eV. This phenomenon is attributed to the strong electronic effect caused by the Schiff base on the surface of cluster **I**, which indicates that cluster **I** has a tendency to transfer electrons to the Schiff base complex during the catalytic process of the composite catalyst. The strong electronic effect between different elements helps to balance the adsorption energy of the reaction intermediates, thus improving the photocatalytic performance.[40]

3.3 UV-visible light absorption test

Fig. 4 shows the UV absorption spectra of the cluster **I**, composite catalysts **I@R1** and **I@R2** (1 : 1 molar ratio), and their maximum absorption wavelengths of visible light are listed in Table 2. The maximum absorption wavelengths of clusters I, **I@R1** and **I@R2** are 493 nm, 411 nm and 490 nm, respectively. Thus, for cluster I, the maximum absorption peaks were blue-shifted by 82 nm and 3 nm when the photosensitizers **R1**{(4-(4-diethylaminophenyl azo) pyridine)} and **R2**(4-styrylpyridine) were added, respectively. The molar absorptivity of **I@R1** increased to 7.6×10^9 L mol^{-1} cm^{-1} (Table 3) due to the strong absorption capacity of the azo group of **R1**. The maximum UV peak and molar absorptivity of the composite catalyst **I@R2** decreased to some extent, as the addition of the 4-styrylpyridine molecule may have caused a change in the charge distribution and local density on the surface of the cluster, thus affecting its absorption spectrum. In addition, 4-styrylpyridine may compete with other molecules in the cluster for absorption, leading to a reduction in the overall absorption peak.

From Fig. 5, it can be seen that the maximum absorption wavelengths of UV visible light absorption of **S1**, **S2** are 397 nm and 485 nm, respectively. When **S1**, **S2** and **I** were mixed in the same molar ratio of 1 : 1, the maximum UV absorption peaks and molar absorptivities of the composite catalysts **I@S1** and **I@S2** were both slightly lower than those of catalysts **S1** and **S2**. This is because the Schiff bases and their complexes are generally weakly basic substances that can interact with the

Table 2 Maximum UV visible light absorption wavelength of the nine catalysts

Entry	Maximum UV visible light absorption wavelength (nm)
I	493
R1	500
R2	420
S1	397
S2	485
I@R1	411
I@R2	490
I@S1	491
I@S2	456

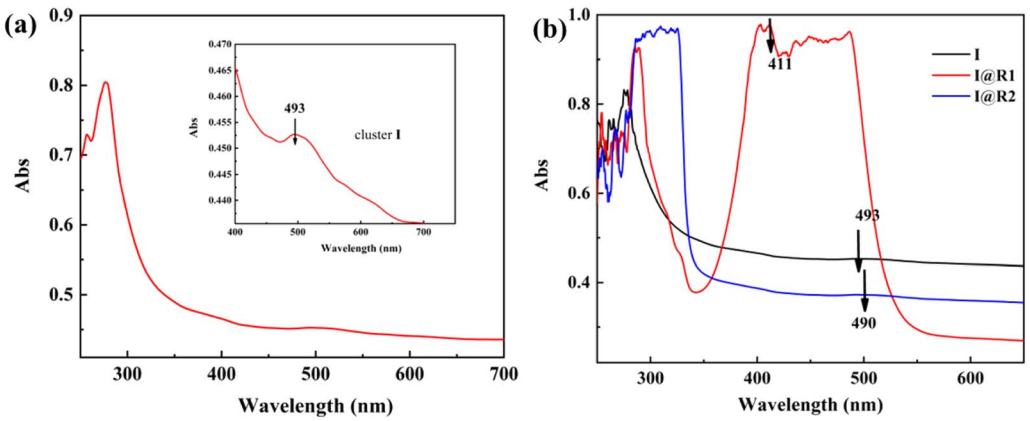

Fig. 4 (a) UV-vis absorption spectrum of 20 μM clusters I in PO (Inset is the enlarged spectrum of clusters I in the visible region). (b) UV-vis absorption spectra of I (black), I@R1 (red) and I@R2 (blue) in PO.

Table 3 Molar absorbance coefficients of the nine catalysts at the maximum visible light absorption wavelength

Entry	Concentration	Absorbancy (l mol^{-1} cm^{-1})	M	Thickness (cm)	Absorptivity (l g^{-1} cm^{-3})	Molar absorptivity (l mol^{-1} cm^{-1})
I	0.25	0.453	1697.2	1	1.812	3.08×10^9
R1	0.25	0.94	254.34	1	3.76	9.56×10^8
R2	0.25	0.01	181.24	1	0.04	7.2×10^6
S1	0.25	0.343	650.27	1	1.372	8.9×10^8
S2	0.25	0.362	645.22	1	1.448	9.34×10^8
I@R1	0.25	0.97	1951.5	1	3.88	7.6×10^9
I@R2	0.25	0.372	1878.4	1	1.488	2.8×10^9
I@S1	0.25	0.227	2347.5	1	0.908	2.1×10^9
I@S2	0.25	0.27	2342.4	1	1.08	2.53×10^9

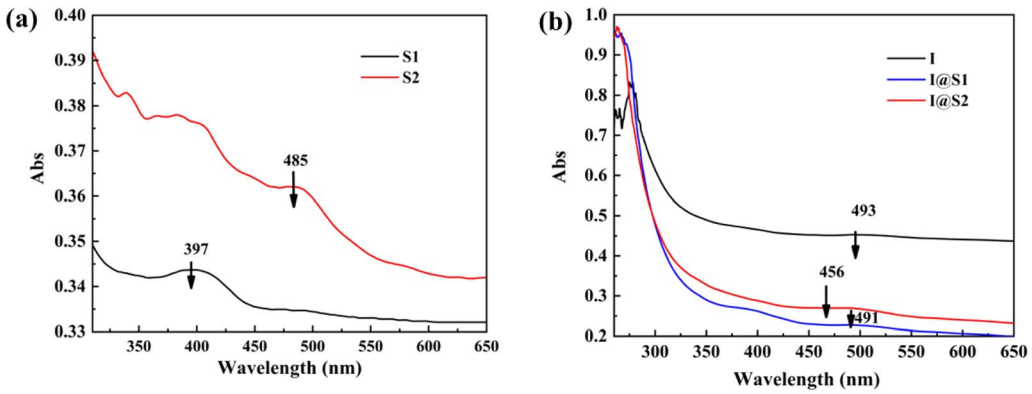

Fig. 5 (a) UV-vis absorption spectra of **S1** (black), **S2** (red). (b) UV-vis absorption spectra of I (black), **I@S1** (red) and **I@S2** (blue) in PO.

nanoclusters. This can lead to a change in the electron density on the surface of the nanoclusters, thus affecting the energy and frequency of their electron jumps, which in turn leads to a change in the position of the absorption peaks of the nanoclusters.

3.4 Copolymerization of CO_2 and PO

The peak at 5.00 ppm in ^{1}H-NMR is due to the production of methyl protons in the polypropylene carbonate (PPC) molecule. As the copolymerization reaction of CO_2 and PO produces different types of products, multiple peaks appear in ^{1}H-NMR. The relative intensities of these peaks can reflect the relative content and selectivity of the different types of products. Fig. 6 shows the ^{1}H-NMR spectra of the copolymerization products of **I** and the four composite catalysts. From the catalytic results (Table 4), it can be seen that cluster **I** has a low selectivity for PPC/CPC when catalyzing the copolymerization of PO and CO_2. This phenomenon may be due to the weak electronic

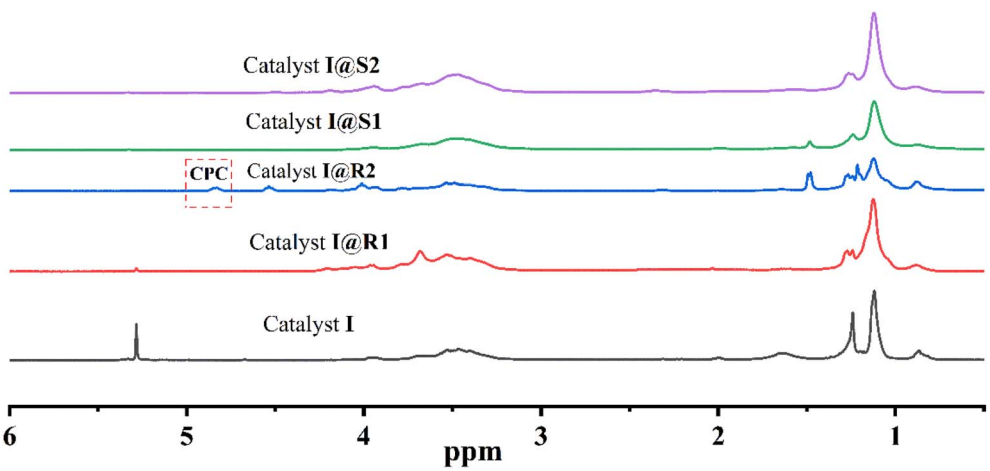

Fig. 6 The ^{1}H-NMR of the copolymerization products for **I**, **I@R1**, **I@R2**, **I@S1** and **I@S2** at 100 W light sources, 60 °C, 6 h and 2 MPa CO_2.

Table 4 CO_2/propylene oxide copolymerization results[a]

Cat	Epoxide	t (h)	P[b] [MPa]	W[c]	TON[d]	PPC (%)	PPO (%)	CPC (%)
I	PO	6	2	0 W	136.5	2.6	94.8	2.6
I	PO	6	2	100 W	137.4	2.87	91	6
[**I@R1**]	PO	6	2	0 W	107.2	5.7	93.4	0.84
[**I@R1**]	PO	6	2	100 W	132.1	6.77	92.2	1
[**I@R2**]	PO	6	2	0 W	159.3	6.31	91.8	1.89
[**I@R2**]	PO	6	2	100 W	229.5	0.72	62.1	37.1
S1	PO	6	2	0 W	166	9.8	86.5	3.7
S1	PO	6	2	100 W	208	8.4	77.5	14.1
S2	PO	6	2	0 W	101	3.1	94.3	2.6
S2	PO	6	2	100 W	129	2.2	90.2	7.6
[**I@S1**]	PO	6	2	0 W	447	19.7	73.5	6.8
[**I@S1**]	PO	6	2	100 W	536.4	16.8	56.8	26.5
[**I@S2**]	PO	6	2	0 W	224	5.6	89.7	4.7
[**I@S2**]	PO	6	2	100 W	237	6.1	78.7	15.2
[**I@S1(1)**]	PO	6	2	100 W	536.4	16.8	56.8	26.4
[**I@S1(3)**]	PO	6	2	100 W	534.7	16.2	55.7	28.1
[**I@S1(5)**]	PO	6	2	100 W	531.8	16.7	56.3	27

[a] Copolymerization condition: PO 10 g, Cat = 3×10^{-6} molar, 60 °C, 2 MPa. [b] CO_2 pressure. [c] Power of external light source, 0 W means there is no external light source. [d] Turnover number: moles of PO consumed per mole of catalyst.

interaction between the oxygen in PO and the manganese around the cluster, resulting in a low selectivity of the catalyst for PPC/CPC.[41]

In order to investigate the relationship between the structure and activity of the clusters, the catalytic effect of the composite catalysts on the copolymerization of CO_2 and PO was studied using cluster I in combination with different photosensitizers. The copolymerization results show that cluster **I** with photosensitizer **R2** containing an electron-withdrawing group exhibits higher selectivity and activity than cluster **I** itself. In the CO_2 and PO copolymerization, when the reaction was carried out at 60 °C under a pressure of 2 MPa CO_2 with a 100 W light source with a specific wavelength, the turnover number (TON) of the catalyst **I@R2** containing a pyridine was 229.5 at 6 h, and the f_{CPC} was 37.1%. When the cluster itself was used to catalyze the copolymerization under the same conditions, its TON was 137.4. When using electron-donating photosensitizers in composite catalytic systems, the difference in activity and selectivity between the catalyst **I@R1** and **I@R2** is more remarkable, and the TON for **I@R1** is 132.1. This is because 4-styrylpyridine has basicity and can react with the acidic CO_2, thus inhibiting the formation of PPO and improving the yield of CPC. The introduction of 4-styrylpyridine in the nanoclusters can regulate the distribution of CO_2 in the reaction system and promote its adsorption and activation on the cluster surface, thus further improving the selectivity of CPC. At the same time, it can be seen that since 1,2-cyclohexanediamine is more flexible than *o*-phenylenediamine, the TON is 208 for S1, whereas the TON is 129 for S2. Because of the interaction between cluster **I** and SalenCo(III), the TON of **I@S1** and **I@S2** is about 2–3 times those of S1 and S2. Due to the weak electronic interaction between *o*-phenylenediamine and the cluster **I**, the selectivity of the catalysts **I@S2** for PPC/CPC is lower than that of **I@S1**. The same phenomenon has been reported by R. Duan *et al.*[21] Moreover, it can be seen from Scheme 3 that compared with the traditional SalenCo(III) catalyst, the catalytic efficiency of pyrrolic N under the boost of the cluster is significantly improved.[42] After the introduction of metal clusters, the TON of **I@S1** increased by nearly 3 times compared with **S1**.

The results show that these transition metal-based nanoclusters also exhibit catalytic activity under mild conditions. Due to the synergistic effect of the Lewis acid site and the Brønsted acidic –COOH groups, the peripheral connection protection ligand (trimethylacetic acid) of cluster **I** exhibits more high catalytic activity. According to previous reports,[43,44] the preliminary mechanism for the cycloaddition of CO_2 and epoxides to cyclic carbonates is believed to be Lewis acid-based catalysis. As shown in Scheme 3, similar to the catalytic process of Schiff base complexes, epoxides were first bound to Lewis acidic Mn/Co sites through oxygen atoms to activate the epoxy ring. Then, the protective ligand (trimethylacetic acid or pyridine) on the surface of the nanoclusters is used as a nucleophilic agent to attack the carbon atoms in the epoxide with low steric resistance, thereby opening the epoxy ring. Subsequently, the opening epoxy ring interacts with CO_2 to form an alkyl carbonate anion, which is converted into the corresponding cyclic carbonate through the final closed-loop step, while the nanocluster **I** is recycled. The high catalytic activity of cluster **I** stems from the synergistic effect of the Brønsted acidic–COOH group binding to the Lewis acidic Mn/Co site.[45] Due to the weak Lewis base sites (nitrogen containing atoms on photosensitizers) in its framework, composite catalyst **I@R2** in the absence of a cocatalyst and light conditions (Table 4) may still lead to low conversion of PO under the same conditions. It can partially activate CO_2 molecules, then attack epoxides attached to Lewis acid sites,[46] and then promote the reaction.

We aim to confirm the multiphase properties of the catalyst. We selected the most catalytically efficient composite catalyst

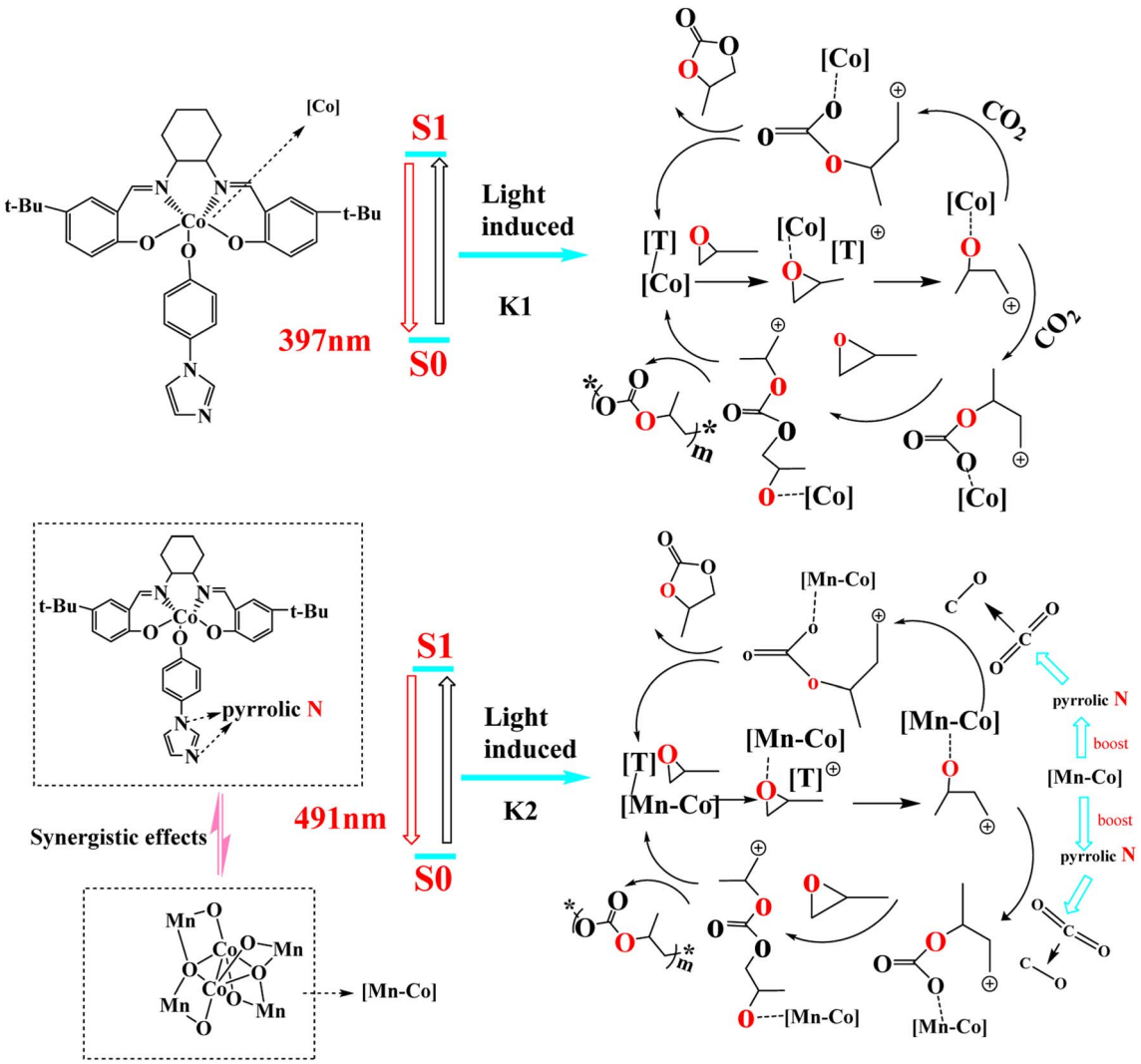

Scheme 3 S1 and I@S1 catalytic copolymerization mechanism of carbon dioxide and PO.

I@S1, and recovery tests showed that **I@S1** was an excellent recoverable catalyst for the solvent-free cycloaddition reaction of CO_2 with epoxide, and that the ^{1}H-NMR of the product (Fig. S8†) after each catalysis was almost identical after several cycles of recovery. The XRD spectrum of the 5th recovered catalyst **I@S1(5)** (Fig. S9†) was almost identical to the fresh one. Combining the thermogravimetric analysis of Fig. S10,† it can be seen that the co-catalysis of nanoclusters and salenCo(III) can complement each other in terms of activity and selectivity, thereby improving the catalytic efficiency. In addition, nanoclusters and salenCo(III) can synergistically improve the catalytic lifetime and stability of the reaction.

4. Conclusions

Such nanoclusters differ from larger nanoparticles because of their quantized energy levels and molecule-like electronic structure. The nanoclusters exhibit enhanced catalytic activity in catalytic reactions. Both the selectivity and catalytic activity of catalyst cluster **I** for PPC/CPC increase with increasing light intensity. It promotes the ring opening of PO, while interacting with CO_2 to promote the cleavage of CO_2 double bonds and the formation of single bonds. When **I** and **R2** co-catalyze the copolymerization of CO_2 and PO in a molar ratio of 1 : 1, the catalytic efficiency is greatly enhanced due to their synergistic effect. The pyridine nitrogen at the end of the photosensitizer is readily excited by the cluster, improving the efficiency of the catalytic CO_2 bond cleavage, while the photosensitizer can act as a co-catalyst, interacting better with the cluster and improving the catalytic efficiency of the catalyst. Similarly, the introduction of metal clusters leads to a significant increase in catalytic efficiency compared to conventional SalenCo(III) catalysts, where the clusters act synergistically with SalenCo(III) *via* pyrrolidine N. **I@S1** increases TON by almost three times compared to **S1**.

Conflicts of interest

There are no conflicts to declare.

Acknowledgements

The authors are thankful for financial support from the Scientific Research Foundation of Education Department of Anhui Province of China (2022AH050103), Anhui Province Key Laboratory of Environment-friendly Polymer Materials, and Key Laboratory of Structure and Functional Regulation of Hybrid Materials (Anhui University), Ministry of Education, Hefei, 230601, PRC.

References

1 D. J. Darensbourg, R. Mackiewicz and J. L. Rodgers, *J. Am. Chem. Soc.*, 2005, **127**, 17565.
2 C. Chen, Z. Zhang, G. Li, L. Li and Z. Lin, *Energy Fuels*, 2021, **35**, 7485–7510.
3 Z. B. Guan, *J. Polym. Sci., Part A: Polym. Chem.*, 2004, **42**, 213–3692.
4 X. Mao, L. Wang, Y. Xu and Y. Li, *J. Phys. Chem. C*, 2020, **124**, 10523–10529.
5 B. Talukdar, S. Mendiratta, M. H. Huang and C.-H. Kuo, *Chem.–Asian J.*, 2021, **16**, 2168–2184.
6 S. Ghosh, E. Gloeckler, C. Woelper, A. Tjaberings, A. H. Groeschel and S. Schulz, *Dalton Trans.*, 2020, **49**, 13475–13486.
7 F. de la Cruz-Martínez, M. Martínez de Sarasa Buchaca, J. Martínez, J. Tejeda, J. Fernández-Baeza, C. Alonso-Moreno, A. M. Rodríguez, J. A. Castro-Osma and A. Lara-Sánchez, *Inorg. Chem.*, 2020, **59**, 8412–8423.
8 R. L. Paddock and S. T. Nguyen, *J. Am. Chem. Soc.*, 2001, **123**, 11498–11499.
9 G. Trott, P. K. Saini and C. K. Williams, *Philos. Trans. R. Soc., A*, 2016, 374.
10 L. Zhu, Y. Dai, B. R. Schrage, C. J. Ziegler and L. Jia, *J. Organomet. Chem.*, 2021, 952.
11 S. Bourrelly, P. L. Llewellyn, C. Serre, F. Millange, T. Loiseau and G. Férey, *J. Am. Chem. Soc.*, 2005, **127**, 13519–13521.
12 A. Buchard, M. R. Kember, K. G. Sandeman and C. K. Williams, *Chem. Commun.*, 2011, **47**, 212–214.
13 R.-L. Duan, Y.-C. Zhou, Z.-Q. Sun, Y.-Z. Huang, X. Pang and X.-S. Chen, *Chin. J. Polym. Sci.*, 2020, **38**, 1124–1130.
14 A. C. Kathalikkattil, R. Babu, J. Tharun, R. Roshan and D.-W. Park, *Catal. Surv. Asia*, 2015, **19**, 223–235.
15 S. Sujith, J. K. Min, J. E. Seong, S. J. Na and B. Y. Lee, *Angew. Chem., Int. Ed.*, 2008, **47**, 7306–7309.
16 W. Qin, S. Long, M. Panunzio and S. Biondi, *Molecules*, 2013, **18**, 12264–12289.
17 C.-H. Ho, H.-J. Chuang, P.-H. Lin and B.-T. Ko, *J. Polym. Sci., Part A: Polym. Chem.*, 2017, **55**, 321–328.
18 M. R. Kember, A. J. P. White and C. K. Williams, *Macromolecules*, 2010, **43**, 2291–2298.
19 Y. Niu and H. Li, *Colloid Polym. Sci.*, 2013, **291**, 2181–2189.
20 S. I. Vagin, R. Reichardt, S. Klaus and B. Rieger, *J. Am. Chem. Soc.*, 2010, **132**, 14367–14369.
21 R. Duan, C. Hu, Z. Sun, H. Zhang, X. Pang and X. Chen, *Green Chem.*, 2019, **21**, 4723–4731.
22 M. R. Kember and C. K. Williams, *J. Am. Chem. Soc.*, 2012, **134**, 15676–15679.
23 R. N. Mukherjea and K. K. Saha, *J. Appl. Polym. Sci.*, 1980, **25**, 2699–2710.
24 M. Scharfenberg, S. Hofmann, J. Preis, J. Hilf and H. Frey, *Macromolecules*, 2017, **50**, 6088–6097.
25 C. H. Tran, S. A. Kim, Y. Moon, Y. Lee, H. M. Ryu, J. H. Baik, S. C. Hong and I. Kim, *Catal. Today*, 2021, **375**, 335–342.
26 K. Nasriddinov, J.-E. Min, H.-G. Park, S. J. Han, J. Chen, K.-W. Jun and S. K. Kim, *Catal. Sci. Technol.*, 2022, **12**, 906–915.
27 X. Chen, X. Ren and X. Gao, *Chin. J. Chem.*, 2022, **40**, 267–274.
28 Q. Wang, S. Wang, X. Hu, F. Li and D. Ling, *Biomater. Sci.*, 2019, **7**, 480–489.
29 Q. Zhang, H. F. Wen, R. Xu, Z. H. Cheng, Y. Sugawara and Y. J. Li, *J. Phys. Chem. C*, 2020, **124**, 28562–28568.
30 J. Yang and R. Jin, *ACS Mater. Lett.*, 2019, **1**, 482–489.
31 Y. Zhang, C. Zhang, C. Xu, X. Wang, C. Liu, G. I. N. Waterhouse, Y. Wang and H. Yin, *Talanta*, 2019, **200**, 432–442.
32 J. Zhao and R. Jin, *Nano Today*, 2018, **18**, 86–102.
33 K. Huang, Q. Li, X.-Y. Zhang, D.-B. Qin and B. Zhao, *Cryst. Growth Des.*, 2022, **22**, 6531–6538.
34 C. Chen, Y. Li, G. Zhao, R. Yao and C. Zhang, *Chemsuschem*, 2017, **10**, 4403–4408.
35 C. Chen, C. Zhang, H. Dong and J. Zhao, *Dalton Trans.*, 2015, **44**, 4431–4435.
36 Z.-J. Liu, X.-L. Wang, C. Qin, Z.-M. Zhang, Y.-G. Li, W.-L. Chen and E.-B. Wang, *Coord. Chem. Rev.*, 2016, **313**, 94–110.
37 C. Chen, C. Zhang, H. Dong and J. Zhao, *Chem. Commun.*, 2014, **50**, 9263–9265.
38 C. Zhang, C. Chen, H. Dong, J.-R. Shen, H. Dau and J. Zhao, *Science*, 2015, **348**, 690–693.
39 C. Chen, Y. Chen, R. Yao, Y. Li and C. Zhang, *Angew. Chem., Int. Ed.*, 2019, **58**, 3939–3942.
40 V. M. Mikoushkin, E. A. Makarevskaya, D. A. Novikov and D. E. Marchenko, *Vacuum*, 2022, **197**, 110849.
41 Y. Hu, L. Du, C. Li, J. Shen, W. Zhu and C. Shao, *J. Chin. Chem. Soc.*, 2020, **67**, 1818–1826.
42 C. He, Y. Zhang, Y. Zhang, L. Zhao, L.-P. Yuan, J. Zhang, J. Ma and J.-S. Hu, *Angew. Chem., Int. Ed.*, 2020, **59**, 4914–4919.
43 Z.-R. Jiang, H. Wang, Y. Hu, J. Lu and H.-L. Jiang, *Chemsuschem*, 2015, **8**, 878–885.
44 A. C. Kathalikkattil, D.-W. Kim, J. Tharun, H.-G. Soek, R. Roshan and D.-W. Park, *Green Chem.*, 2014, **16**, 1607–1616.
45 L. Liu, S.-M. Wang, Z.-B. Han, M. Ding, D.-Q. Yuan and H.-L. Jiang, *Inorg. Chem.*, 2016, **55**, 3558–3565.
46 J. Kim, S.-N. Kim, H.-G. Jang, G. Seo and W.-S. Ahn, *Appl. Catal., A*, 2013, **453**, 175–180.